

Cite this: *Nanoscale*, 2019, **11**, 8579

## High-speed scanning ion conductance microscopy for sub-second topography imaging of live cells†

Stefan Simeonov and Tilman E. Schäffer  \*Received 17th December 2018,  
Accepted 6th April 2019

DOI: 10.1039/c8nr10162k

rsc.li/nanoscale

Scanning ion conductance microscopy (SICM) is an emerging tool for non-invasive and high-resolution topography imaging of live cells. However, the imaging speed of conventional SICM setups is slow, requiring several seconds or even minutes per image, thereby making it difficult to study cellular dynamics. Here, we describe a high-speed SICM (HS-SICM) setup for topography imaging in the hopping mode with a pixel rate of 11.0 kHz, which is 15 times faster than what was reported before. In combination with a "turn step" procedure for rapid pipette retraction, we image the ultra-fast morphodynamics of live human platelets, A6 cells, and U2OS cells at a rate as fast as 0.6 s per frame. The results show that HS-SICM provides a useful platform for investigating the dynamics of cell morphology on a sub-second timescale.

## Introduction

Rapid changes in cell morphology are of central importance for dynamic cellular functions such as the invasion of cancer cells,<sup>1</sup> immune surveillance of T cells,<sup>2</sup> and adhesion and activation of human platelets.<sup>3,4</sup> Imaging of such morphodynamics improves our understanding of the underlying cytoskeletal processes in cells<sup>5</sup> and their interaction with the environment.<sup>6</sup> In the past, several techniques have been used to quantify live cell morphology under physiological conditions. The most established technique for visualizing live cells with high temporal resolution is optical microscopy. However, the spatial resolution of classical optical microscopy is diffraction-limited. Super-resolution optical microscopy overcomes this limit<sup>7</sup> but requires labeling the cells with fluorophores. Atomic force microscopy (AFM) can be used to observe morphological dynamics of live cells<sup>8,9</sup> with high spatial and temporal resolution<sup>10,11</sup> without requiring labeling. The application of a mechanical force by the AFM cantilever tip, however, may pose a physiological stimulus that affects cell behavior<sup>12,13</sup> or may even damage the cell membrane.<sup>14,15</sup>

Scanning ion conductance microscopy (SICM) is a scanning probe technique based on an electrolyte-filled nanopipette through which an ion current is driven.<sup>16</sup> This current serves as a measure for the pipette-sample distance and allows for label-free, non-contact topography imaging. Over the past years, SICM has become a powerful and versatile tool for non-

invasive and high-resolution imaging of live cells,<sup>15,17–19</sup> artificial membranes,<sup>20</sup> and single proteins.<sup>21</sup>

In the prevalent hopping/backstep imaging mode, approach curves are acquired by recording the ion current while approaching the pipette toward the sample. When a preset current trigger value is detected, indicating close proximity between pipette and sample, the position of the z-piezo is recorded and the pipette is retracted.<sup>19,22,23</sup> By repeating this procedure at many positions across the sample, an image of sample topography is generated. For conventional SICM setups, the acquisition time is on the order of minutes,<sup>24</sup> which hampers the investigation of highly dynamic processes such as cellular endocytosis,<sup>24</sup> particle uptake,<sup>25</sup> microvilli movement,<sup>26</sup> and platelet morphodynamics.<sup>27</sup>

Over the past decade, researchers have developed several approaches to reduce the acquisition time for SICM imaging. Novak *et al.* reported an adaptive algorithm that varies the local pixel density and hop distance depending on the local roughness of the sample surface.<sup>19</sup> Shevchuk *et al.* introduced a combination of a large-range piezo with a fast, small-range shear piezo to quickly retract the pipette from the sample when the current trigger occurs, thereby avoiding mechanical contact and allowing for an acquisition time of 7 s per frame.<sup>24</sup> The reported approach velocities in both studies were  $\approx 0.10 \text{ mm s}^{-1}$ . Gesper *et al.* recently used this method of combined piezos with approach velocities of  $0.65 \text{ mm s}^{-1}$  in single approach curves.<sup>28</sup> Jung *et al.* described a current-controlled feedback mechanism that reduces the approach velocity of the pipette when getting close to the sample surface, thereby avoiding mechanical contact at an initial approach velocity of  $0.30 \text{ mm s}^{-1}$ .<sup>29</sup> Ida *et al.* optimized the hop distance to reduce unnecessary and time consuming vertical motion by detecting pipette-sample contact during lateral movements, achieving an acquisition

Institute of Applied Physics, University of Tübingen, Auf der Morgenstelle 10, 72076 Tübingen, Germany. E-mail: tilman.schaeffer@uni-tuebingen.de

† Electronic supplementary information (ESI) available: Fig. S1–S4, Movies 1–6. See DOI: 10.1039/c8nr10162k

time of 18 s per frame while using an approach velocity of up to  $0.50 \text{ mm s}^{-1}$  on live cells.<sup>30</sup> The reported approach rates (*i.e.*, pixel rates) in all these studies were in the range of 72–230 Hz. Seifert *et al.* imaged the morphodynamics of live platelets with an approach velocity of  $0.34 \text{ mm s}^{-1}$ , an approach rate of 256 Hz and an acquisition time of 4 s per frame.<sup>27</sup> Watanabe and Ando used a small-range scanner to achieve an approach velocity of up to  $0.40 \text{ mm s}^{-1}$  and an approach rate of 714 Hz when imaging a calibration grid at 3.5 s per frame.<sup>31</sup>

Here, we describe a high-speed SICM (HS-SICM) setup utilizing an extremely fast scanner with a maximum scan range of  $21 \mu\text{m} \times 21 \mu\text{m}$  (in *xy*-direction) and  $5 \mu\text{m}$  (in *z*-direction). By using this setup, together with a “turn step” procedure that significantly reduces the vertical overshoot distance, we recorded topography images at an approach rate of 11.0 kHz – by far the highest approach rate reported to date. This allowed us to follow the ultra-fast morphodynamics of live human platelets, A6 cells, and U2OS cells with an acquisition time as fast as 0.6 s per frame.

## Results and discussion

### HS-SICM setup

We built a HS-SICM setup (Fig. 1a) that allows for hopping mode imaging rates fifteen times faster compared to previous HS-SICM setups.<sup>27,30,31</sup> The setup consists of a custom-made *xy* and *z* sample scanner on which a small culture dish is

mounted (see Experimental section for details). The nanopipette is held stationary over the sample by a spring-loaded holder for comfortable access to the sample and fast and easy pipette exchange. This miniaturized configuration allowed us to reduce the inertial mass that is moved by the *z*-piezo (*i.e.*, the sample holder filled with electrolyte) to only 0.6 g, thereby providing a fast mechanical response. In comparison, the corresponding inertial mass in our “conventional” setup utilizing a *z*-flexure stage is 39 g. We note that a large-range *z*-piezo that is combined with a fast, small-range shear piezo<sup>24</sup> has the advantage of offering large approach velocities without sacrificing range. We also note that optical access to the sample, potentially combined with fluorescence microscopy, has not yet been implemented in our high-speed setup. Optical access could be achieved by using an objective with a large working distance or by converting the setup to a pipette-scanning configuration, as in a recently presented high-speed SICM setup,<sup>31</sup> in combination with an inverted optical microscope.

For HS-SICM topography measurements in the hopping mode (Fig. 1b), the sample is approached towards the pipette at a high velocity (here:  $v_{\text{Appr}} = 2.95 \text{ mm s}^{-1}$ ). When the sample is in close proximity to the pipette tip (trigger position) such that a preset current trigger  $I_{\text{Trig}}$  (here:  $I_{\text{Trig}}/I_0 = 0.98$ , where  $I_0$  is the free ion current when the sample is far off the pipette) occurs (at trigger time  $t_{\text{Trig}}$ ), the sample needs to be retracted rapidly to avoid mechanical contact. This is achieved by reversing the *z*-drive signal (Fig. 1b, upper graph, dashed green

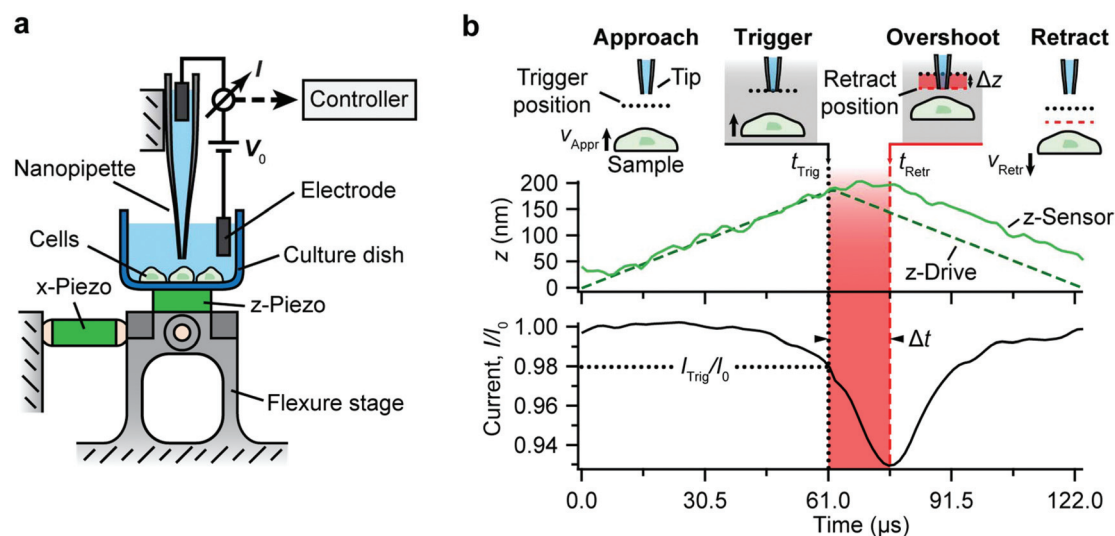


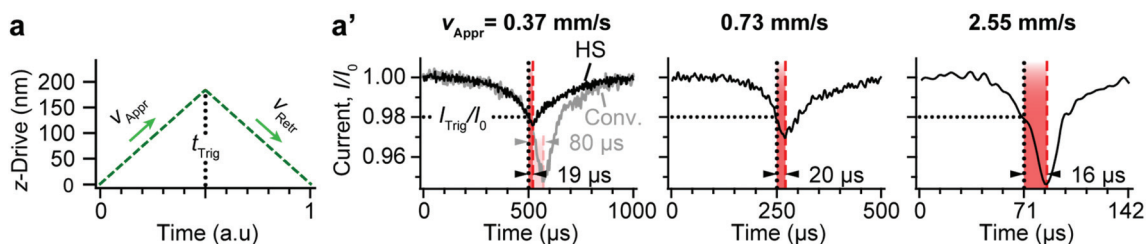
**Fig. 1** (a) Schematic of the HS-SICM setup consisting of a stationary nanopipette mounted on top of an *xy* and *z* sample scanner. The sample scanner consists of an *x*-piezo and a *y*-piezo (out of the image plane) pushing against a flexure stage and of a *z*-piezo on which a culture dish is mounted. An applied voltage  $V_0$  between two electrodes induces an ion current  $I$  through the electrolyte-filled nanopipette. A controller records this ion current and drives the *xy*- and *z*-piezos. (b) Time course of the sample's *z*-position (upper graph) and of the ion current (lower graph) during an approach curve in the hopping mode (here: approach rate of 8 kHz). The sample is vertically approached towards the nanopipette tip with a velocity  $v_{\text{Appr}}$  (here:  $v_{\text{Appr}} = 2.95 \text{ mm s}^{-1}$ ). At the trigger position, where a preset current trigger ( $I_{\text{Trig}}/I_0$ , dotted horizontal line in lower graph) occurs at the trigger time  $t_{\text{Trig}}$  (dotted vertical line; here:  $t_{\text{Trig}} = 61 \mu\text{s}$ ). The controller then inverts the slope of the *z*-piezo drive signal (kink in green dashed line in upper graph) to retract the sample from the nanopipette. Owing to the finite response time of the *z*-piezo and to signal delay, the sample does not revert its direction immediately but continues approaching the tip for an “overshoot time”  $\Delta t$  (red bar and black arrowheads; here:  $\Delta t = 15 \mu\text{s}$ ) until the sample is at the position physically closest to the tip (“retract position”), indicated by the minimum of the current at the retract time  $t_{\text{Retr}}$  (red dashed line; here:  $t_{\text{Retr}} = 76 \mu\text{s}$ ).

curve). The z-sensor signal (solid green curve) and the measured ion current (lower graph) show that the sample continues to approach the tip for a short period of time after the trigger occurred (overshoot time  $\Delta t$ , red bar in graph), until the ion current is minimum at the time of closest approach ( $t_{\text{Retr}}$ ). The sample then physically retracts from the tip, indicated by the increasing ion current. The presence of an overshoot time  $\Delta t = t_{\text{Retr}} - t_{\text{Trig}}$  is owing to the inertial mass of the moving components (e.g., the sample), to the limited power output of the piezo amplifier (and thus implicitly to the capacitance of the z-piezo), to the pipette capacitance, and to the bandwidth in which the current signal is detected.

### Hopping mode with turn step

We tested the performance of the z-piezo of our HS-SICM setup by recording the ion current and the z-position of the sample as a function of time for different approach velocities. In regular hopping mode, the approach velocity is reversed when the current trigger occurs (Fig. 2a). A larger approach velocity  $v_{\text{Appr}}$  gives a larger decrease of the ion current below the current trigger level (Fig. 2a'). The overshoot time  $\Delta t$  (black arrowheads) is 16–20  $\mu\text{s}$ , independent of the approach velocity. For comparison, we show a corresponding approach curve recorded with our “conventional” SICM setup (Fig. 2a', gray

### Hopping mode



### Hopping mode with turn step

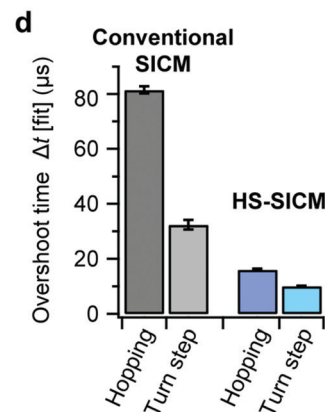
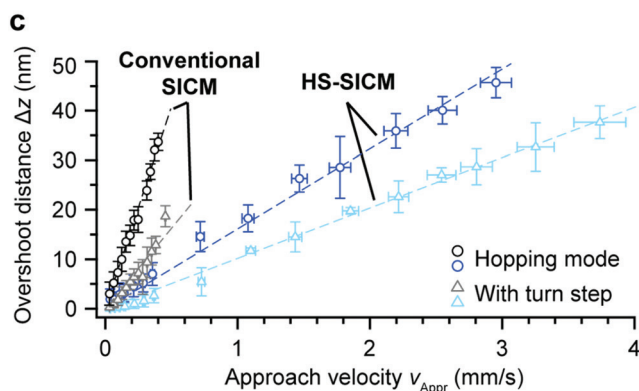
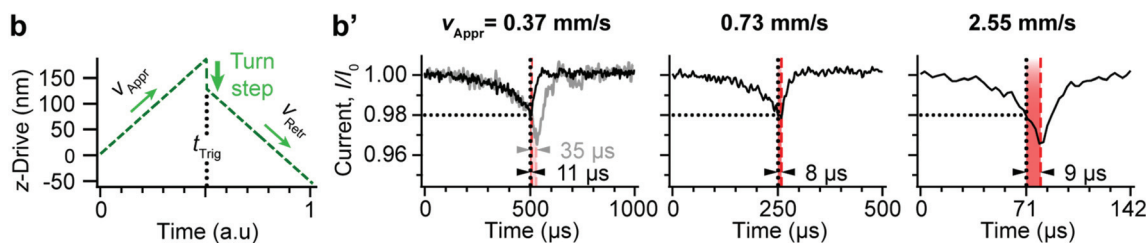


**Fig. 2** Evaluation of the overshoot distance and the overshoot time in the hopping mode using the HS-SICM setup. Time course of approach curves at different approach velocities  $v_{\text{Appr}}$  in hopping mode without (a, a') and with (b, b') a turn step (here: turn step size of 65 nm) applied to the z-piezo when the current trigger occurs at time  $t_{\text{Trig}}$  (vertical black dotted lines). With increasing approach velocity the overshoot time (black arrowheads) stays about constant, but the ion current decreases more below the current trigger level, indicating an increasing overshoot distance. In the case of the turn step (b, b'), the overshoot time  $\Delta t$  is significantly reduced. The conventional SICM setup (gray traces) exhibits a significantly larger overshoot time  $\Delta t$  (gray arrowheads). (c) Overshoot distance  $\Delta z$  (approximated as  $\Delta z \approx v_{\text{Appr}} \times \Delta t$ ) as a function of  $v_{\text{Appr}}$  for hopping mode without (circles) and with turn step (triangles). The HS-SICM setup (blue colors) exhibits significantly lower vertical overshoot compared to the conventional SICM setup (gray colors). Line fits (dashed lines) suggest a linear relation between  $\Delta z$  and  $v_{\text{Appr}}$ . Each data point represents the mean value from 2500 approach curves. (d) Overshoot time (slope from fit shown in panel c). A smaller overshoot time reduces the risk of mechanical contact between sample and tip and therefore allows for faster scanning. Error bars denote standard deviation (c) or fit error (d).

trace) – note the much larger decrease of the ion current and the much larger overshoot time.

To achieve an even faster response of the *z*-piezo in the HS-SICM setup, we modified the hopping mode by applying a step function (“turn step”) to the *z*-piezo when the current trigger occurs (Fig. 2b). This turn step decreased the overshoot time  $\Delta t$  by a factor of two to 8–11  $\mu\text{s}$  (Fig. 2b', black arrow-heads), compared to the data without the turn step (Fig. 2a'). For the conventional SICM setup, the turn step decreased the overshoot time from 80  $\mu\text{s}$  to 35  $\mu\text{s}$  (Fig. 2a' and b', gray traces). The idea of quickly retracting the pipette when the current trigger occurs was addressed previously,<sup>24,28</sup> but those solutions required an additional *z*-piezo.

We optimized the turn step size by increasing it to the point just before image distortions became visible (such as cross-coupling between the *z*- and *xy*-piezos). The optimized turn step size was  $\approx 10$ –70 nm for the pipettes used in this study. Increasing the turn step size beyond 70 nm did not further decrease the overshoot time  $\Delta t$  (ESI Fig. S1 and S2†).

We approximated the corresponding overshoot distance as  $\Delta z \approx v_{\text{Appr}} \times \Delta t$  and plotted  $\Delta z$  as a function of the approach velocity  $v_{\text{Appr}}$  (measured from the slope of the *z*-sensor data) (Fig. 2c). Blue and gray colors denote data collected with the HS-SICM setup and with our fastest conventional SICM setup, respectively, recorded with identical hopping mode settings for fair comparison. The overshoot distance was significantly reduced for a given approach velocity when using hopping mode with turn step instead of regular hopping mode for both the high-speed and the conventional SICM setup (Fig. 2c). The data suggest a linear relationship between  $\Delta z$  and  $v_{\text{Appr}}$  in all four cases. We have applied line fits  $\Delta z \approx v_{\text{Appr}} \times \Delta t$  (dashed lines in Fig. 2c) to estimate the average overshoot time  $\Delta t$  (slope of the line fit) (Fig. 2d). The average overshoot time for the conventional SICM setup was 82  $\mu\text{s}$  in regular hopping mode and 32  $\mu\text{s}$  in hopping mode with turn step. The HS-SICM setup had significantly lower average overshoot times (16  $\mu\text{s}$  and 10  $\mu\text{s}$ , respectively). Therefore, using a small-range *z*-piezo decreased the overshoot time by a factor of  $\approx 5$ , and using the turn step additionally decreased the overshoot time by a factor of  $\approx 2$ . We obtained similar results for different pipettes (within the specified radius range) and for different current trigger values ( $I_{\text{Trig}}/I_0 \geq 0.98$ ). The overshoot time is affected only by the mechanical response of the *z*-piezo and by the time delay in detecting the current trigger.

To warrant non-contact topography imaging, the overshoot distance should not exceed the pipette-sample distance at the trigger position. This distance depends on the nanopipette's inner opening radius  $r_i$  and the preset current trigger. Both a smaller opening radius and a smaller current trigger give a smaller pipette-sample distance at the trigger position. According to Fig. 4 in Rheinlaender and Schäffer,<sup>32</sup> we estimate the pipette-sample distance as  $\approx 0.6 \times r_i = 50$  nm (using a pipette opening radius of  $\approx 80$  nm) when using a current trigger of  $I_{\text{Trig}}/I_0 = 0.98$ . The approach velocity could therefore be set up to 5.0  $\text{mm s}^{-1}$  for this pipette in the HS-SICM setup using the turn step procedure while still providing non-contact

measurements (example approach curves recorded with an approach velocity of  $v_{\text{Appr}} = 4.8 \text{ mm s}^{-1}$  in regular hopping mode and in hopping mode with turn step are shown in Fig. S3†).

The spatial resolution depends on the pipette opening radius, where smaller radii give a better resolution.<sup>33</sup> The opening radius, on the other hand, affects the maximum possible approach velocity: a pipette with a smaller opening radius needs to be approached slower to avoid mechanical pipette-sample contact after the trigger occurs (assuming an unchanged overshoot time). This is because the pipette-sample distance at trigger time is smaller for a pipette with a smaller radius, but the overshoot distance is unchanged.

The approach rate (= temporal resolution) depends on the approach velocity and on the hop distance. The hop distance has to be chosen depending on the sample's local height differences. Larger height differences require a larger hop distance to avoid mechanical pipette-sample contact, thereby reducing the approach rate.

### Performance evaluation of the HS-SICM setup

To evaluate the imaging performance of our HS-SICM setup, we recorded topography images of a calibration grid at different approach rates (Fig. 3). The grid is accurately imaged up to an approach rate of 11.0 kHz. Representative height profiles along the red dotted lines (Fig. 3b, profiles are aligned for better visibility) are in good agreement with the nominal dimensions of the calibration grid (58 nm height,  $2 \mu\text{m} \times 2 \mu\text{m}$  periodic pattern). We quantified the image quality by calculating the standard deviation of the images (Fig. 3c) with respect to a reference image (top left image, see Experimental section). The standard deviation for the images recorded at approach rates of 0.2–8.5 kHz is  $\approx 10$  nm. This value represents the regular SICM image noise. The slightly increased standard deviation of 12 nm at 11.0 kHz (Fig. 3c, black arrow) indicates the onset of slight image distortions, mainly near the left margin of the corresponding image. At 11.7 kHz (Fig. 3c, red arrow), larger distortions obscure the grid pattern. These distortions are likely owing to the first lateral resonant frequency of the sample scanner at  $\approx 12$  kHz (Fig. 2 in Braunsma and Schäffer<sup>34</sup>).

### High-speed imaging of human platelets

We recorded a high-speed topography image sequence of the highly dynamic periphery of a live platelet over a time span of 10 min at a rate of 0.6 s per frame (approach rate 2.0 kHz) (Fig. 4b and ESI Movie 1† containing 1000 consecutive images). The region of the image sequence is marked in the overview image (Fig. 4a, red box). Small protrusions formed and propagated at the platelet edge (arrows in Fig. 4b) at velocities between 100  $\text{nm s}^{-1}$  and 300  $\text{nm s}^{-1}$ . These images demonstrate that high-speed imaging is necessary for an accurate detection and tracking of the rapidly changing cell morphology (additional movies are provided as ESI Movies 2 and 3†). A similar protrusion morphodynamics was observed before but with a lower temporal resolution in platelets<sup>27</sup> and



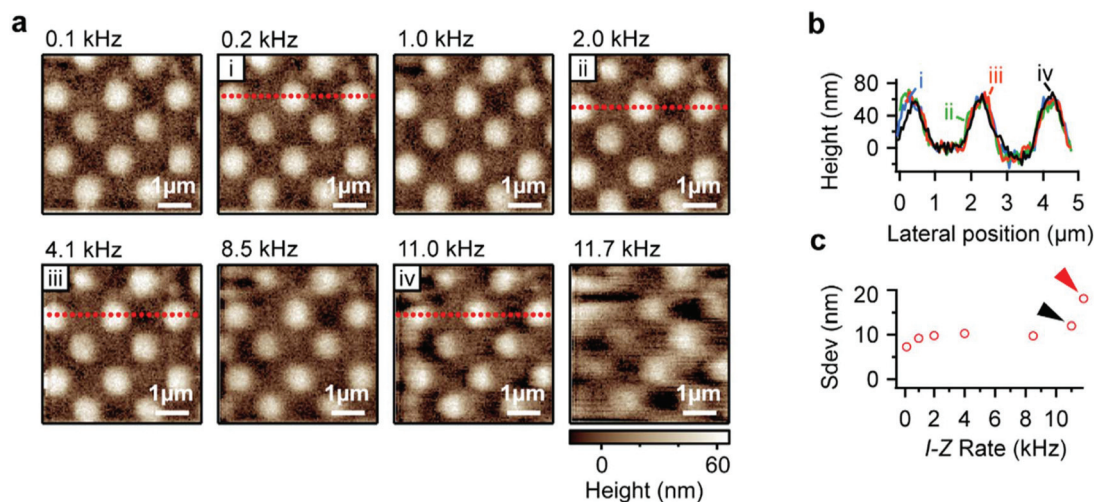


**Fig. 3** (a) Topography images of a calibration grid replica recorded at different approach rates with HS-SICM. The grid is accurately imaged at approach rates up to 11.0 kHz. At higher approach rates (11.7 kHz), distortions are visible. (b) Height profiles (aligned) along the red dotted lines in panel a are almost identical and indicate accurate surface tracking even at an approach rate of 11.0 kHz. (c) Standard deviation of the (aligned) images in panel a with respect to a reference image (here: the image recorded at 0.1 kHz) (see Experimental section). A value of  $\approx 10$  nm represents the regular SICM imaging noise (0.1–8.5 kHz). A slightly larger value (12 nm) at 11.0 kHz (black arrow) marks the onset of imaging artifacts in the form of slight distortions, mainly near the left margin of the corresponding image in panel a. At 11.7 kHz, larger distortions are detected (red arrow). The images were recorded with  $100 \times 100$  pixels. Approach velocity  $v_{\text{Appr}}$  was between  $0.01 \text{ mm s}^{-1}$  (0.1 kHz) and  $1.21 \text{ mm s}^{-1}$  (11.7 kHz).

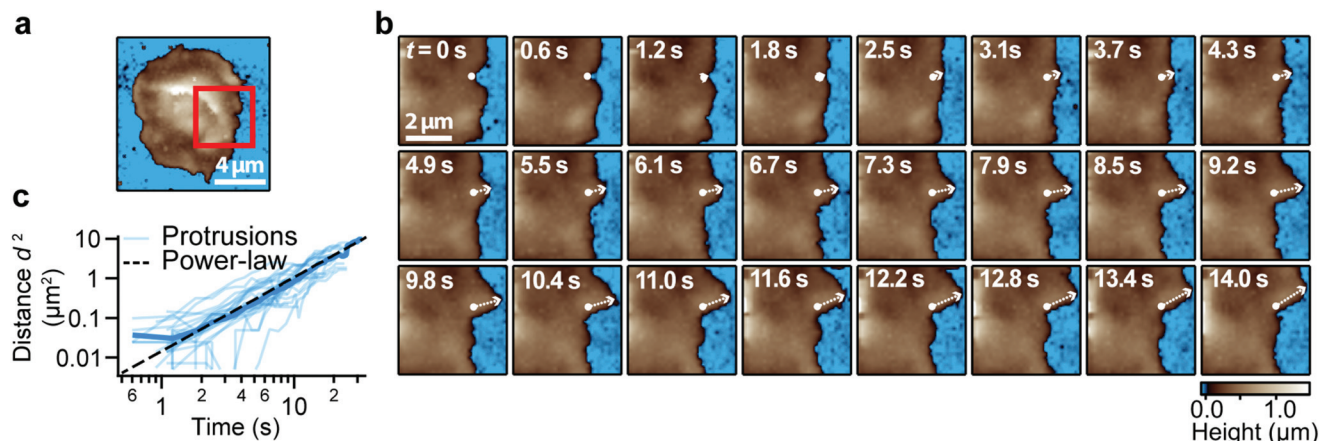


**Fig. 4** (a) Overview image of a live platelet and (b) high-speed image sequence of the dynamics of the platelet periphery imaged with HS-SICM in the red outlined area. The image sequence (0.6 s per frame) shows rapid morphological changes along the platelet edge on the sub-second time-scale (arrows). Small protrusions form and move along the platelet edge. The white arrow indicates the distance between the starting point of the protrusion (dot) and its current position (arrowhead). (c) Squared distance for different protrusions (thin curves) and mean squared distance (bold curve). The mean squared distance shows a power-law behavior in time (dashed line). The full image sequence (1000 images in 10 min) is provided as ESI (Movie 1†). Images were recorded with  $64 \times 64$  pixels (overview) and  $32 \times 32$  pixels (sequence) at an approach rate of 0.25 kHz and 2 kHz, respectively. The approach velocity  $v_{\text{Appr}}$  was  $0.35 \text{ mm s}^{-1}$  (overview) and  $1.40 \text{ mm s}^{-1}$  (sequence).

in nucleated cells,<sup>35,36</sup> and was associated with actin polymerization. We measured the mean squared distance  $d^2$  of different protrusions ( $n = 22$  from 4 different platelets) as a function of time  $t$  (Fig. 4c) and applied a power-law fit  $d^2 = c \times t^\alpha$  (dashed line in Fig. 4c) with pre-factor  $c$  and power-law exponent  $\alpha$ . The fit gave  $\alpha = 1.9 \pm 0.03$ , indicating a more directed motion of the protrusions ( $\alpha = 2$  for directed motion,  $\alpha = 1$  for a random walk).<sup>37</sup> The same power-law exponent for the dynamics of platelet protrusions was observed before.<sup>27</sup> As a

control, we imaged a whole platelet at a rate of 4.3 s per frame for 25 min before and 18 min after fixation (ESI Fig. S4 and Movie 4† containing 600 consecutive images). The fixation stopped the fast dynamics at the platelet periphery.

#### High-speed imaging of A6 cells

We recorded a high-speed topography image sequence of microvilli on a live *Xenopus laevis* kidney epithelial A6 cell at a rate of 1.4 s per frame (approach rate: 2.94 kHz) (Fig. 5a and

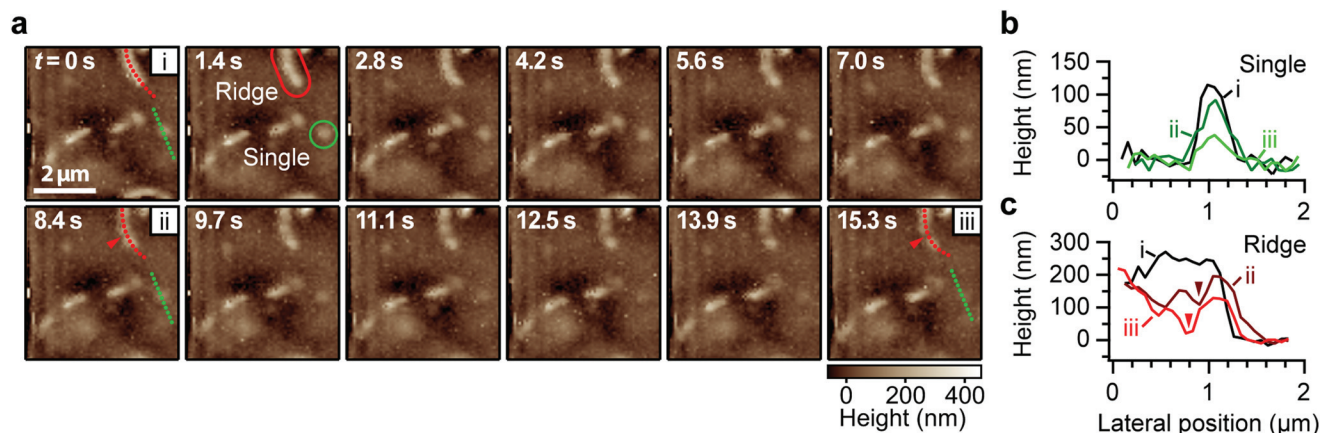


**Fig. 5** (a) High-speed image sequence of the dynamics of a live A6 cell surface imaged with HS-SICM. The image sequence (1.4 s per frame) shows ridge-like organized (red outline) and single (green outline) microvilli. (b) Height profiles of a single microvillus along the green dotted lines in panel a. The microvillus gradually retracts from the cell surface. (c) Height profiles of a ridge-like microvillus along the red dashed lines in panel a. At time  $t = 0$  s (i), no individual microvilli are identified within the ridge. At  $t = 8.4$  s (ii), a gradually increasing dip appears on the ridge (red arrowhead), and at  $t = 15.3$  s (iii), a single microvillus (at lateral position 1.1  $\mu\text{m}$ ) has separated from the ridge. The entire separation process is visible at the beginning of the full image sequence (100 images in 2.3 min), provided as ESI (Movie 5†). Images were recorded with  $64 \times 64$  pixels at an approach rate of 2.94 kHz. The approach velocity  $v_{\text{Appr}}$  was  $2.68 \text{ mm s}^{-1}$ .

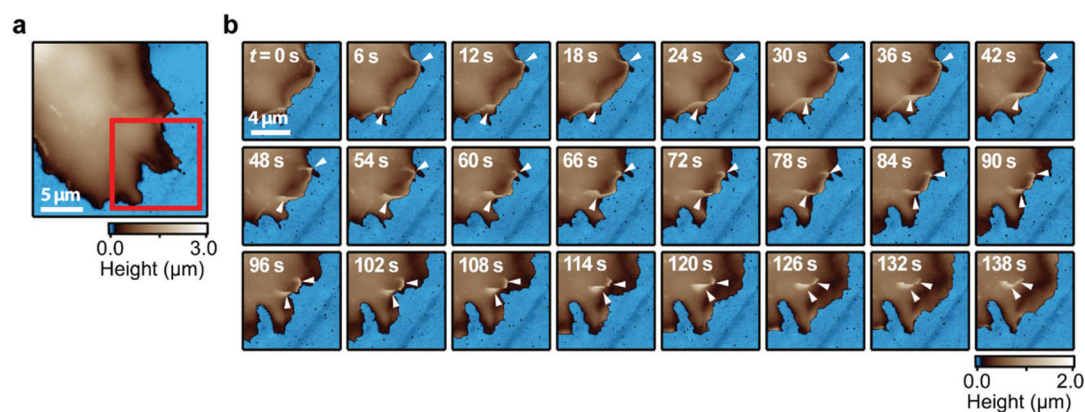


**Fig. 6** (a) Overview image of a live U2OS cell and (b) high-speed image sequence of the dynamics of the cell periphery imaged with HS-SICM in the red outlined area. The image sequence (6 s per frame) shows rapid morphological changes of the cell. Large membrane protrusions (arrowheads) form at the cell edge and propagate across the cell in a wave-like motion. The full image sequence (1000 images in 100 min) is provided as ESI (Movie 6†). Images were recorded with  $100 \times 100$  pixels at an approach rate of 1.0 kHz (overview) and 1.67 kHz (sequence). The approach velocity  $v_{\text{Appr}}$  was  $1.50 \text{ mm s}^{-1}$  (overview) and  $1.88 \text{ mm s}^{-1}$  (sequence).

ESI Movie 5† containing 100 consecutive images). The sequence revealed numerous, highly dynamic microvilli with a width between 250–400 nm, a height below 500 nm, and a length between 250 nm and several micrometers. While some microvilli grew, others retracted, some within seconds (Fig. 5a and b). The ridge-like microvillar structures are comprised of single microvilli.<sup>15,26,30</sup> We resolved the spontaneous separation of single microvilli from a ridge-like microvillar structure within seconds (Fig. 5a and c, arrowheads).

### High-speed imaging of U2OS cells

We recorded a high-speed topography image sequence of an osteosarcoma U2OS cell at a rate of 6 s per frame (approach rate: 1.67 kHz) (Fig. 6 and ESI Movie 6† containing 1000 con-

secutive images). Large membrane protrusions with a height between 300–800 nm (Fig. 6b, arrowheads) formed at the cell edge and then propagated across the cell in a wave-like motion.

## Conclusion

We developed a sample-scanning HS-SICM setup with a travel range of 21  $\mu\text{m}$  in  $xy$ -direction and 5  $\mu\text{m}$  in  $z$ -direction. Our setup exhibits a fast response of the  $z$ -piezo to the  $z$ -drive signal, leading to an overshoot time of  $\Delta t = 16 \mu\text{s}$  in regular hopping mode. By applying a “turn step” procedure, we were able to reduce this overshoot time to  $\Delta t = 10 \mu\text{s}$ . The vertical overshoot

distance  $\Delta z$  is proportional to the approach velocity  $v_{\text{Appr}}$  and thus to the overshoot time  $\Delta t$  ( $\Delta z \approx v_{\text{Appr}} \times \Delta t$ ). To warrant non-contact topography imaging, the approach velocity should be adjusted so that the overshoot distance  $\Delta z$  does not exceed the pipette-sample distance at the trigger time.

The SICM images shown in this study were recorded in combination with a turn step procedure and an approach velocity of up to  $v_{\text{Appr}} = 2.68 \text{ mm s}^{-1}$ , which is 6-fold faster than the largest approach velocities in SICM imaging reported to date.<sup>30,31</sup> We recorded approach curves using even faster approach velocities of up to  $v_{\text{Appr}} = 4.8 \text{ mm s}^{-1}$  without damaging the nanopipette, which is promising for further advances in HS-SICM imaging.

Our setup allowed high-speed topography imaging of a small calibration grid replica at an approach rate of 11.0 kHz. According to our knowledge, this is faster by a factor of fifteen than the highest published approach rate so far. We also recorded high-speed topography image sequences of live human platelets, A6 cells, and U2OS cells at a rate as fast as 0.6 s per frame, which is eightfold faster than the fastest frame rate on a biological sample reported so far.<sup>27</sup> We anticipate that HS-SICM will become a useful platform for high-speed investigations of live cells.

## Experimental

### SICM setups

The HS-SICM setup (Fig. 1a) consisted of a custom-built sample scanner based on a small aluminum flexure stage with a width of 10 mm and a height of 13 mm. For  $xy$ -positioning of the sample, two piezoelectric stack actuators ( $x$ - and  $y$ -piezos) (PSt 150/5×5/20, Piezomechanik GmbH, München, Germany) were preloaded against the flexure stage. By applying a voltage to the piezos, the stage was pushed sideways, thereby elastically bending its legs. For  $z$ -positioning of the sample a low-capacitance piezoelectric stack actuator ( $z$ -piezo) (NAC2012-H06, Noliac, Kvistgaard, Denmark) was glued on top of the flexure stage. The piezo capacitances were  $C_{xy} = 1.85 \text{ }\mu\text{F}$  and  $C_z = 95 \text{ nF}$ . The scan range of the setup was  $21 \text{ }\mu\text{m}$  in  $xy$ -direction and  $5 \text{ }\mu\text{m}$  in  $z$ -direction. The piezo extensions were measured with strain gauges. A detailed description of the scanner can be found elsewhere.<sup>34</sup> The sample holder (a small culture dish) was attached to the  $z$ -piezo by a small amount of quick-drying varnish. A small pipette holder (spring-loaded clip), which held the nanopipette stationary over the sample, was mounted onto three motorized micrometer screws for automated coarse approach of the pipette using a stepper motor.

The “conventional” SICM setup consisted of a  $200 \text{ }\mu\text{m}$   $xy$ -scanner (P-542.2CL, Physik Instrumente, Karlsruhe, Germany) for lateral positioning of the sample and a  $15 \text{ }\mu\text{m}$   $z$ -scanner (P-753.11C, Physik Instrumente) for vertical positioning of the pipette.<sup>27</sup> The conventional SICM setup was mounted on an inverted optical microscope (Ti-U, Nikon, Tokyo, Japan) for optical inspection of the pipette and the sample.

In both setups, the ion current was measured by a wide-band and low-noise current amplifier (NF-SA605-F2, NF Corporation, Yokohama, Japan) utilizing a low-pass filter set to 100 kHz.

Nanopipettes with a typical inner opening radius ( $r_i$ ) of 80–100 nm were fabricated with a  $\text{CO}_2$ -laser-based pipette puller (P-2000, Sutter Instruments, Novato, CA). The ratio of a pipette's inner opening radius ( $r_i$ ) and outer opening radius ( $r_o$ ) was  $r_o/r_i \approx 1.5$ , and the half opening angle was  $\alpha_{\text{pipette}} \approx 3^\circ$ .

The inner opening radius was determined by fitting a numerical model to the ion current as a function of vertical pipette position.<sup>32</sup> The achievable lateral resolution depends on the inner opening radius  $r_i$  and can be estimated<sup>33</sup> as  $\approx 3r_i$ , giving a lateral resolution of 240–300 nm in our measurements. Ag/AgCl electrodes were made from silver wire that was immersed in a sodium hypochlorite solution for 30 min.

### Imaging parameters

The images in Fig. 3 were recorded in hopping mode with turn step using a nanopipette with an opening radius of  $r_i \approx 100 \text{ nm}$ . The preset current trigger was set to  $I_{\text{Trig}}/I_0 = 0.99$  (*i.e.*, 1% below the free ion current  $I_0$  when the sample is far off the pipette), leading to a pipette-sample distance at the trigger time of about 100 nm ( $\approx 1.0 \times r_i$ ).<sup>32</sup> The turn step size was 20 nm and the hop distance was 57 nm.

The image sequence of a live platelet (Fig. 4) was recorded in hopping mode with turn step 3 min after the overview image. The preset current trigger was set to  $I_{\text{Trig}}/I_0 = 0.993$ , leading to a pipette-sample distance at the trigger time of about 120 nm ( $\approx 1.5 \times r_i$ )<sup>32</sup> (nanopipette with  $r_i \approx 80 \text{ nm}$ ). The approach velocity was  $v_{\text{Appr}} = 1.40 \text{ mm s}^{-1}$  and the turn step size was 35 nm. The hop distance was 700 nm for the overview image and 350 nm for the sequence.

The image sequence of a live A6 cell (Fig. 5) was recorded in hopping mode with turn step. The preset current trigger was set to  $I_{\text{Trig}}/I_0 = 0.9935$ . The approach velocity was  $v_{\text{Appr}} = 2.68 \text{ mm s}^{-1}$ , the approach rate was 2.94 kHz, the turn step size was 50 nm, and the hop distance was 450 nm.

The image sequence of a live U2OS cell (Fig. 6) was recorded in hopping mode with turn step. The preset current trigger was set to  $I_{\text{Trig}}/I_0 = 0.991$ . The approach velocity was  $v_{\text{Appr}} = 1.50 \text{ mm s}^{-1}$  for the overview image and  $v_{\text{Appr}} = 1.88 \text{ mm s}^{-1}$  for the sequence; the approach rate was 1.0 kHz and 1.67 kHz, respectively. The turn step size was 50 nm. The hop distance was 750 nm for the overview image and 560 nm for the sequence.

### Cell culture and sample preparation

For HS-SICM measurements, we cut out small polystyrene culture dishes from a 96 well “TC”-treated (“culture treated”) culture plate (Cellstar Microplates, Greiner Bio-One, Frickenhausen, Germany) and cut the height of the culture dishes to 6 mm using a red hot knife. For “conventional” SICM measurements, “TC”-treated (“tissue culture”) polystyrene culture dishes (Cellstar Petri Dishes, Greiner Bio-One) were used. The data shown in Fig. 2 were recorded on uncoated



culture dishes, filled with phosphate-buffered saline (PBS) (L1820, Biochrom, Berlin, Germany).

In Fig. 3, we used a polydimethylsiloxane (PDMS) (Sylgard 186, Dow Corning, MI, USA) replica of a calibration grating (UMG02, Anfatec Instruments AG, Oelsnitz, Germany) that had a  $2\ \mu\text{m} \times 2\ \mu\text{m}$  periodic pattern with 58 nm high and (rounded)  $1\ \mu\text{m} \times 1\ \mu\text{m}$  wide features. Measurements were performed in PBS.

Human platelets were isolated from freshly drawn blood of healthy volunteers as described elsewhere.<sup>27</sup> All procedures were approved by the institutional ethics committee (237/2018BO2) and comply with the declaration of Helsinki. Informed consent was obtained from all participants. The culture dishes were coated with collagen ( $10\ \mu\text{g cm}^{-2}$ , Takeda, Linz, Austria). About  $10^8$  of the freshly isolated platelets were added to the culture dish containing 150  $\mu\text{L}$  of Tyrode-HEPES buffer (136.89 mM NaCl, 2.68 mM KCl, 1.05 mM  $\text{MgCl}_2$ , 0.42 mM  $\text{NaH}_2\text{PO}_4$ , 11.9 mM  $\text{NaHCO}_3$ , 1 mM  $\text{CaCl}_2$ ,  $1\ \text{g L}^{-1}$  D-glucose,  $1\ \text{g L}^{-1}$  bovine serum albumin (BSA), 4 mM HEPES, pH 6.5) and were allowed to adhere for 2–10 min. The samples were then washed with Tyrode-HEPES buffer three times to remove cell debris and non-adherent platelets directly before HS-SICM measurements (Fig. 4). During measurements, Tyrode-HEPES buffer was used as culture medium. Platelet fixation (ESI Fig. S4 and Movie 4†) was done by adding formaldehyde (Sigma-Aldrich, St Louis, MO) and glutaraldehyde (Carl Roth GmbH+Co. KG, Germany, Karlsruhe) to the culture medium to a final concentration of 2% and 1%, respectively.

*Xenopus laevis* epithelial A6 cells were cultured at 28 °C and 1%  $\text{CO}_2$ . The culture medium consisted of 35% v/v Leibovitz L-15 medium (Life Technologies, Carlsbad, CA), 35% v/v Hams F-12 medium (Life Technologies), 18.9% v/v sterile water, 0.3% v/v sodium bicarbonate solution (7.5% water) (Life Technologies), 9.1% v/v fetal calf serum (Life Technologies), 1.7% v/v L-glutamine solution (200 mM stock solution) (K0283, Sigma-Aldrich), and 1% v/v penicillin/streptomycin (10 000 U  $\text{mL}^{-1}$  stock solution) (K2213, Sigma-Aldrich). Measurements were performed in Leibovitz L-15 medium.

Human tibia osteosarcoma U2OS cells were cultured at 37 °C and 5%  $\text{CO}_2$ . The culture medium consisted of Gibco DMEM (Life Technologies), supplemented with 10% v/v fetal calf serum (Life Technologies), 2% v/v L-glutamine solution (200 mM stock solution) (K0283, Sigma-Aldrich), and 1% v/v penicillin/streptomycin (10 000 U  $\text{mL}^{-1}$  stock solution) (K2213, Sigma-Aldrich). Measurements were performed in Leibovitz L-15 medium.

### Data analysis and statistics

Data processing and analysis were carried out with Igor Pro (Wavemetrics, Portland, OR). For calculation of the parameters  $\Delta t$ ,  $t_{\text{Trig}}$ , and  $t_{\text{Retr}}$ , simple threshold detection was used. No smoothing or averaging of the ion current data was done. The approach velocity  $v_{\text{Appr}}$  was calculated from the average slope of the z-sensor data from many curves.

The topography images from Fig. 3 were flattened using a fifth order plane fit to correct for local bending of the soft

PDMS grid replica. The topography images from Fig. 4, 5 and 6 were flattened using a first, third, and first order plane fit, respectively. The power-law fit in Fig. 4c was obtained by weighting with the data points' standard error of the mean.

For quantitative analysis of the topography images (Fig. 3b and c), we first chose a high-quality reference image (here: the image recorded at 0.1 kHz approach rate, top left). Then we automatically aligned the other images (recorded at higher approach rates) to this reference image using a self-written 2D fit algorithm to correct for lateral and vertical drift. The observed shift of the image features to the right at larger approach rates (Fig. 3a) is owing to the finite response time of the x-piezo. We calculated the standard deviation of the height values of the difference between an aligned image and the reference image as a quantitative measure of image quality. The standard deviation represents a combination of imaging errors comprised of the typical SICM imaging noise and the misrepresentation of the topography image due to imaging artifacts.

### Conflicts of interest

There are no conflicts to declare.

### Acknowledgements

Funded by the Deutsche Forschungsgemeinschaft (DFG, German Research Foundation) – Projektnummer 374031971 – TRR-240 and by the DFG KFO-274.

### References

- 1 A. G. Clark and D. M. Vignjevic, *Curr. Opin. Cell Biol.*, 2015, **36**, 13–22.
- 2 E. Cai, K. Marchuk, P. Beemiller, C. Beppler, M. G. Rubashkin, V. M. Weaver, A. Gerard, T.-L. Liu, B.-C. Chen, E. Betzig, F. Bartumeus and M. F. Krummel, *Science*, 2017, **356**, eaal3118.
- 3 R. D. Allen, L. R. Zacharski, S. T. Widirstky, R. Rosenstein, L. M. Zaitlin and D. R. Burgess, *J. Cell Biol.*, 1979, **83**, 126–142.
- 4 D. Lee, K. P. Fong, M. R. King, L. F. Brass and D. A. Hammer, *Biophys. J.*, 2012, **102**, 472–482.
- 5 A. Mogilner and K. Keren, *Curr. Biol.*, 2009, **19**, R762–R771.
- 6 B. Geiger, J. P. Spatz and A. D. Bershadsky, *Nat. Rev. Mol. Cell Biol.*, 2009, **10**, 21–33.
- 7 B. Huang, H. Babcock and X. Zhuang, *Cell*, 2010, **143**, 1047–1058.
- 8 M. Radmacher, R. W. Tillmann, M. Fritz and H. E. Gaub, *Science*, 1992, **257**, 1900–1905.
- 9 Y. F. Dufrène, T. Ando, R. Garcia, D. Alsteens, D. Martinez-Martin, A. Engel, C. Gerber and D. J. Müller, *Nat. Nanotechnol.*, 2017, **12**, 295.
- 10 C. Braunsman, J. Seifert, J. Rheinlaender and T. E. Schäffer, *Rev. Sci. Instrum.*, 2014, **85**, 073703.



- 11 M. Shibata, H. Watanabe, T. Uchihashi, T. Ando and R. Yasuda, *Biophys. Physicobiol.*, 2017, **14**, 127–135.
- 12 M. Fritz, M. Radmacher and H. E. Gaub, *Exp. Cell Res.*, 1993, **205**, 187–190.
- 13 K. Haase and A. E. Pelling, *J. R. Soc., Interface*, 2015, **12**, 20140970.
- 14 H. X. You, J. M. Lau, S. Zhang and L. Yu, *Ultramicroscopy*, 2000, **82**, 297–305.
- 15 J. Seifert, J. Rheinlaender, P. Novak, Y. E. Korchev and T. E. Schäffer, *Langmuir*, 2015, **31**, 6807–6813.
- 16 P. K. Hansma, B. Drake, O. Marti, S. A. Gould and C. B. Prater, *Science*, 1989, **243**, 641–643.
- 17 C.-C. Chen, Y. Zhou and L. A. Baker, *Annu. Rev. Anal. Chem.*, 2012, **5**, 207–228.
- 18 Y. E. Korchev, C. L. Bashford, M. Milovanovic, I. Vodyanoy and M. J. Lab, *Biophys. J.*, 1997, **73**, 653–658.
- 19 P. Novak, C. Li, A. I. Shevchuk, R. Stepanyan, M. Caldwell, S. Hughes, T. G. Smart, J. Gorelik, V. P. Ostanin, M. J. Lab, G. W. J. Moss, G. I. Frolenkov, D. Klenerman and Y. E. Korchev, *Nat. Methods*, 2009, **6**, 279–281.
- 20 M. Böcker, S. Muschter, E. K. Schmitt, C. Steinem and T. E. Schäffer, *Langmuir*, 2009, **25**, 3022–3028.
- 21 A. I. Shevchuk, G. I. Frolenkov, D. Sánchez, P. S. James, N. Freedman, M. J. Lab, R. Jones, D. Klenerman and Y. E. Korchev, *Angew. Chem., Int. Ed.*, 2006, **45**, 2212–2216.
- 22 S. A. Mann, G. Hoffmann, A. Hengstenberg, W. Schuhmann and I. D. Dietzel, *J. Neurosci. Methods*, 2002, **116**, 113–117.
- 23 P. Happel and I. D. Dietzel, *J. Nanobiotechnol.*, 2009, **7**, 7.
- 24 A. I. Shevchuk, P. Novak, M. Taylor, I. A. Diakonov, A. Ziyadeh-Isleem, M. Bitoun, P. Guicheney, J. Gorelik, C. J. Merrifield and D. Klenerman, *J. Cell Biol.*, 2012, **197**, 499–508.
- 25 P. Novak, A. Shevchuk, P. Ruenraroengsak, M. Miragoli, A. J. Thorley, D. Klenerman, M. J. Lab, T. D. Tetley, J. Gorelik and Y. E. Korchev, *Nano Lett.*, 2014, **14**, 1202–1207.
- 26 J. Gorelik, A. I. Shevchuk, G. I. Frolenkov, I. A. Diakonov, M. J. Lab, C. J. Kros, G. P. Richardson, I. Vodyanoy, C. R. Edwards, D. Klenerman and Y. E. Korchev, *Proc. Natl. Acad. Sci. U. S. A.*, 2003, **100**, 5819–5822.
- 27 J. Seifert, J. Rheinlaender, F. Lang, M. Gawaz and T. E. Schäffer, *Sci. Rep.*, 2017, **7**, 4810.
- 28 A. Gesper, P. Hagemann and P. Happel, *Nanoscale*, 2017, **9**, 14172–14183.
- 29 G.-E. Jung, H. Noh, Y. K. Shin, S.-J. Kahng, K. Y. Baik, H.-B. Kim, N.-J. Cho and S.-J. Cho, *Nanoscale*, 2015, **7**, 10989–10997.
- 30 H. Ida, Y. Takahashi, A. Kumatani, H. Shiku and T. Matsue, *Anal. Chem.*, 2017, **89**, 6015–6020.
- 31 S. Watanabe and T. Ando, *Appl. Phys. Lett.*, 2017, **111**, 113106.
- 32 J. Rheinlaender and T. E. Schäffer, *Anal. Chem.*, 2017, **89**, 11875–11880.
- 33 J. Rheinlaender and T. E. Schäffer, *Anal. Chem.*, 2015, **87**, 7117–7124.
- 34 C. Brauns mann and T. E. Schäffer, *Nanotechnology*, 2010, **21**, 225705.
- 35 M. Machacek and G. Danuser, *Biophys. J.*, 2006, **90**, 1439–1452.
- 36 T. Bretschneider, K. Anderson, M. Ecke, A. Müller-Taubenberger, B. Schroth-Diez, H. C. Ishikawa-Ankerhold and G. Gerisch, *Biophys. J.*, 2009, **96**, 2888–2900.
- 37 R. Metzler and J. Klafter, *J. Phys. A: Math. Gen.*, 2004, **37**, R161.